Monotonicity-based Electrical Impedance Tomography for Lung Imaging

Liangdong Zhou*, Bastian Harrach†, and Jin Keun Seo*
*Department of Computational Science & Engineering, Yonsei University, Korea
†Department of Mathematics, University of Stuttgart, Germany.

arXiv:1702.02563v1 [q-bio.QM] 8 Feb 2017

***Abstract*—This paper presents a monotonicity-based spatiotemporal conductivity imaging method for continuous regional lung monitoring using electrical impedance tomography (EIT). The EIT data (i.e., the boundary current-voltage data) can be decomposed into pulmonary, cardiac and other parts using their different periodic natures. The time-differential current-voltage operator corresponding to the lung ventilation can be viewed as either semi-positive or semi-negative definite owing to monotonic conductivity changes within the lung regions. We used this monotonicity constraints to improve the quality of lung EIT imaging. We tested the proposed methods in numerical simulations, phantom experiments and human experiments.**

***Index Terms*—Electrical impedance tomography, continuous lung monitoring, monotonicity, inverse problem, monotonicity-based regularization**

I. Introduction

ELECTRICAL impedance tomography (EIT) has received much recent attention owing to its unique ability to allow long-term, continuous monitoring of lung ventilation at the bedside [2], [3], which is not possible using other medical imaging techniques such as computerized tomography (CT), magnetic resonance imaging (MRI), ultrasound (US), or single photon emission computed tomography (SPECT). The increasing sophistication of monitoring intensive-care patients might incorporate the use of EIT system to guide strategies for protective lung ventilation via the close monitoring of patient's lung [7], [12], [13], [28], [30], [34], [43]. Although EIT cannot compete with CT, MRI or ultrasound in terms of spatial resolution or accuracy [23], its ability to provide long-term, continuous monitoring and portability make it clinically useful.

This paper focuses mainly on the lung EIT. In EIT, multiple surface electrodes are attached to an imaging object to inject currents and measure boundary voltages. At frequencies below about 250 kHz, the potential induced by the injection current is dictated approximately by the elliptic partial differential equation $\nabla \cdot (\sigma \nabla u) = 0$ inside the object where σ is the time-varying conductivity distribution associated with lung ventilation [23], [35]. The measured EIT data can be viewed as a boundary current-voltage map from the injection current to the resulting boundary voltage, which is determined mainly by the effective conductivity distribution, the configuration of the surface electrodes, and the geometry of the imaging object. Lung EIT aims to provide dynamic images of the time-differential conductivity distribution from the time-differential current-voltage map while minimizing the forward modeling errors due to such as electrode position, boundary geometry, and uncertainty of the reference conductivity distribution.

Robust EIT reconstruction algorithms have been sought since the invention of the first EIT devices by Barber and Brown in the early 1980s [1], [5], [6], [33]. However, EIT is not yet suitable for routine clinical use because of its poor sensitivity [39]. Robust reconstruction may rely on incorporating some strong prior information into the algorithm via regularization. Unfortunately, it seems inadequate to achieve robust time difference EIT reconstructions only with regularization, such as Tikhonov regularization [35], [40] and total variation regularization [8], in spatial domain. In other words, temporal regularization should be used with the prior information in time domain, especially for time difference EIT.

Taking into account of the fundamental limitation of EIT, some strong prior information about the individual's pulmonary function needs to be incorporated into the analysis along with the measured data. We know that the time-varying patterns in lung EIT data depend mainly on the pulmonary and cardiac cycles and diaphragm motion. Given that the pulmonary and cardiac cycles have different frequencies, we can extract patterns corresponding to the ventilation from the measured EIT data by eliminating the signals associated with cardiac motion and other processes [14], [29].

Using the extracted ventilation-induced signals, we apply the characteristic of monotonicity to the regional lung imaging. This is based on the assumption that changes of conductivity distribution induced by lung ventilation are either monotonically non-increasing or monotonically non-decreasing at any fixed time. This assumption can be understood in terms of the effective conductivity, which means the overall conductivity changes induced by ventilation can be regarded as monotonically non-increasing or monotonically non-decreasing. An increase of conductivity decreases the voltage measurements in terms of matrix definiteness. In other words, if the conductivity increases between two time frames, the measured difference data matrix should be negative semi-definite. Conversely, a conductivity decrease would increase the voltage measurements in terms of matrix definiteness. We observe that the time-derivative of the current-voltage data associated with ventilation is a non-negative operator during inhalation and a non-positive operator during exhalation.

We therefore enforce a global non-positivity constraint on

Manuscript received date; revised date; Corresponding author: Bastian Harrach (email:harrach@math.uni-frankfurt.de).

the reconstructed conductivity changes during inhalation, and a global non-negativity constraint during exhalation, which is named as global monotonicity-based method (GMM). Moreover, on each pixel, we derive a local lower bound during inhalation (and a local upper bound during exhalation) using a sensitivity-based variant of the linearized monotonicity method for inclusion detection [20], [37], [38], which is named as local monotonicity-based method (LMM). Enforcing the monotonicity constraints in the image reconstruction algorithm can compensate for the inherent ill-conditioned nature of EIT [4]. The effectiveness of the proposed GMM is validated by numerical simulations, phantom experiments and human experiments while LMM is tested only by numerical simulations and phantom experiments.

II. Methods

A. Mathematical model

Let an imaging object occupy a two- or three-dimensional region $\Omega \subset \mathbb{R}^n$ $(n = 2, 3)$. We denote the time-varying conductivity at position x and time t by $\sigma^t(x)$. In E-channel EIT system as shown in Fig. 1 (a), we attach E electrodes $\mathcal{E}_1, \mathcal{E}_2, \cdots, \mathcal{E}_E$ on its boundary $\partial\Omega$ to inject E different currents ($E-1$ linearly independent) using orderly chosen pairs of electrodes. For the ease of explanation, we use the adjacent pair of electrodes $\mathcal{E}_j$ and $\mathcal{E}_{j+1}$ to inject j-th current. Here and in the following, we use the convention that $\mathcal{E}_{E+1} = \mathcal{E}_1$. Then, the distribution of the voltage subject to the j-th injection current, denoted by u_t^j, is governed by the following complete electrode model [36], [41]

$$\begin{cases} \nabla \cdot \left(\sigma^t \nabla u_t^j\right) = 0 & \text{in } \Omega, \\ \sigma^t \frac{\partial u_t^j}{\partial \mathbf{n}} = 0 & \text{on } \partial\Omega \setminus \bigcup_{k=1}^{E} \mathcal{E}_k, \\ \left(u_t^j + z_{j,k}\sigma^t \frac{\partial u_t^j}{\partial \mathbf{n}}\right)\Big|_{\mathcal{E}_k} = U^{j,k}(t), \quad k = 1, \ldots, E & \\ \int_{\mathcal{E}_k} \sigma^t \frac{\partial u_t^j}{\partial \mathbf{n}}\, ds = 0 \quad \text{if } k \in \{1, \ldots, E\} \backslash \{j, j+1\}, & \\ \int_{\mathcal{E}_j} \sigma^t \frac{\partial u_t^j}{\partial \mathbf{n}}\, ds = I = -\int_{\mathcal{E}_{j+1}} \sigma^t \frac{\partial u_t^j}{\partial \mathbf{n}}\, ds, & \end{cases} \tag{1}$$

where $\mathbf{n}$ is the outward unit normal vector on $\partial\emptyset$, $U^{j,k}$ is the voltage on $\mathcal{E}_k$, and $z_{j,k}$ is the contact impedance of the k-th electrode $\mathcal{E}_k$. The magnitude of the current driven through the j-th and the $(j+1)$-th electrode is assumed to be normalized to $I = 1$. The solution u_t^j is unique up to constant factors.

Assuming that the boundary voltages between all adjacent pairs of electrodes are measured, the k-th boundary voltage measured between $\mathcal{E}_k$ and $\mathcal{E}_{k+1}$ subject to the j-th injection current is the time-varying function

$$V^{j,k}(t) = U^{j,k}(t) - U^{j,k+1}(t), \tag{2}$$

where $k, j = 1, 2, \ldots, E$. Thus, we collect E^2 number of time-varying boundary data which can be expressed as the following matrix form

$$\mathbb{V}(t) = \begin{bmatrix} V^{1,1}(t) & \cdots & V^{1,E}(t) \\ V^{2,1}(t) & \cdots & V^{2,E}(t) \\ \vdots & \ddots & \vdots \\ V^{E,1}(t) & \cdots & V^{E,E}(t) \end{bmatrix}. \tag{3}$$

The inverse problem of lung EIT for monitoring the ventilation is to visualize the time varying distribution of σ^t in the lung regions from the time-varying data $\mathbb{V}(t)$.

B. Boundary data separation

It is reasonable to assume $z_{j,k}\sigma^t \frac{\partial u_t^j}{\partial \mathbf{n}} \approx 0$ on the voltage sensing electrodes in (1), so that we have $u_t^j|_{\mathcal{E}_k} = U^{j,k}(t)$ for $|k-j| > 1$. Therefore, for $|k-j| > 1$, the conductivity is related to the measured signals by the following identities

$$V^{j,k}(t) = \int_\Omega \sigma^t \nabla u_t^j \cdot \nabla u_t^k dx, \tag{4}$$

$$\frac{d}{dt} V^{j,k}(t) = -\int_\Omega \frac{\partial \sigma^t}{\partial t} \nabla u_t^j \cdot \nabla u_t^k dx, \tag{5}$$

which are proven in the Appendix A.

However, the unknown contact impedances of current-driven electrodes are not ignorable. The measurements on the current-driven electrodes are affected by the unknown contact impedances. Therefore, the identities (4) and (5) fail for $|k-j| \leq 1$.

The potentials u_t^j and u_t^k are related to the unknown conductivity σ^t via (1). Standard linearized reconstruction methods (LM) [35] for EIT replace u_t^j and u_t^k on the right hand side of (5) by reference potentials and solve the resulting linear equation to determine $\frac{\partial \sigma^t}{\partial t}$ from $\frac{d}{dt} V^{j,k}(t)$.

In this work, we will propose two monotonicity-based improvements to this standard linearized reconstruction method. The first improvement is based on the following data separation approach. We decompose the time-derivative of the conductivity $\frac{\partial}{\partial t}\sigma^t(x)$ at position x into two parts

$$\frac{\partial}{\partial t}\sigma^t(x) = \frac{\partial}{\partial t}\sigma_L^t(x) + \frac{\partial}{\partial t}\sigma_H^t(x) \quad x \in \Omega, \tag{6}$$

where $\frac{\partial}{\partial t}\sigma_L^t$ and $\frac{\partial}{\partial t}\sigma_H^t$ are conductivity change induced by the lung ventilation, cardiac activities and other factors, respectively.

For the application of lung monitoring, we are interested in recovering the ventilation-induced conductivity change $\frac{\partial \sigma_L^t}{\partial t}$. Hence, we postulate the existence of a ventilation-induced signal

$$V_L^{j,k}(t) = \int_\Omega \sigma_L^t \nabla u_t^j \cdot \nabla u_t^k dx, \tag{7}$$

and aim to extract

$$\frac{d}{dt} V_L^{j,k}(t) = -\int_\Omega \frac{\partial \sigma_L^t}{\partial t} \nabla u_t^j \cdot \nabla u_t^k dx, \tag{8}$$

from $\frac{d}{dt} V^{j,k}(t)$. Similar as (3), the ventilation-induced data can be written as an $E \times E$ matrix

$$\mathbb{V}_L(t) = \begin{bmatrix} V_L^{1,1}(t) & \cdots & V_L^{1,E}(t) \\ V_L^{2,1}(t) & \cdots & V_L^{2,E}(t) \\ \vdots & \ddots & \vdots \\ V_L^{E,1}(t) & \cdots & V_L^{E,E}(t) \end{bmatrix}. \tag{9}$$

The ventilation-induced signals $V_L^{j,k}(t)$ can be obtained by applying band-pass filter to the measured data $V^{j,k}(t)$ with a selected frequency range. Because the frequency spectrum of

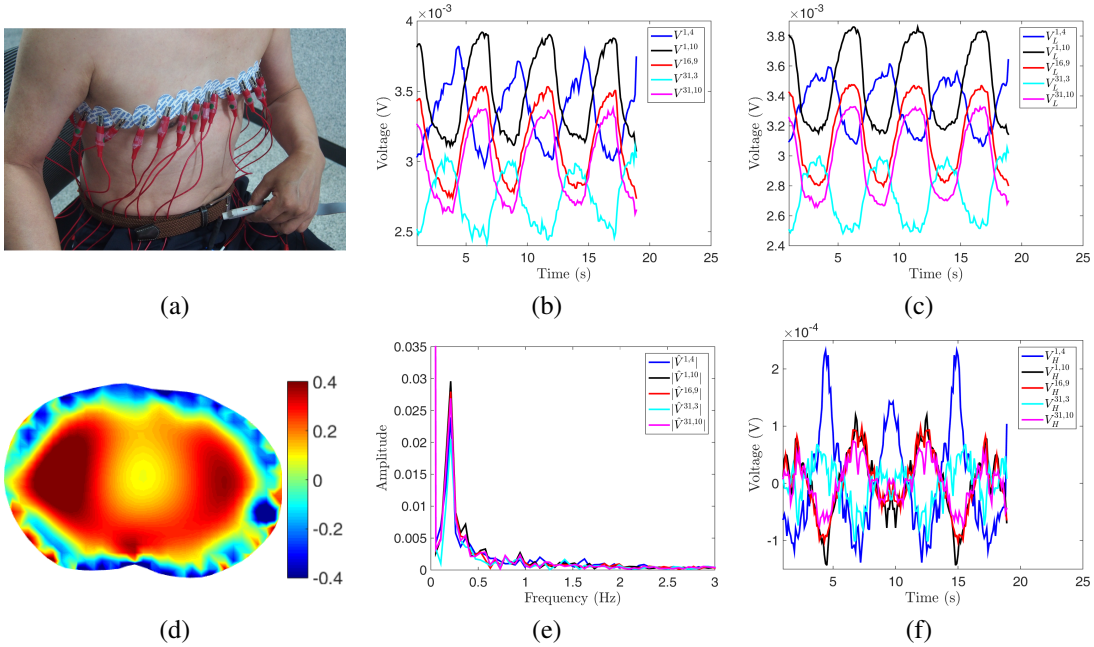

Figure 1. EIT data provided by 32-channel Swisstom EIT system with 4 skipped injection pattern. In this special pattern, $V^{j,k}$ denotes the voltage difference between $\mathcal{E}_k$ and $\mathcal{E}_{k+5}$ subject to the injection current using the pair $\mathcal{E}_j$ and $\mathcal{E}_{j+5}$. (a) electrodes configuration; (b) measured boundary data $V^{j,k}$; (c) low frequency component $V_L^{j,k}$; (d) reconstructed conductivity image using the standard LM; (e) Fast Fourier transform $\hat{V}^{j,k}$; (f) high frequency component $V_H^{j,k}$.

the ventilation signals is much different from that of cardiac signals, data separation can be done based on the Fast Fourier Transform. Fig. 1 shows a human experiment. We see that the separated ventilation-induced signals in Fig. 1 (c) is periodic and monotonically changing in the period of inhalation and exhalation. Fig. 1 (f) shows the high frequency component $V_H^{j,k}$ which is corresponding to the cardiac activities, measurement noise and other factors. The cardiac signal peak is not obviously shown in Fig. 1 (e) because the cardiac signal is significantly smaller in amplitude compare with the ventilation-induced signal.

C. Monotonicity constraints

After extracting the ventilation-induced signals $V_L^{j,k}(t)$ from the measured signals using a band-pass filter, we can reconstruct the ventilation-induced conductivity change $\frac{\partial \sigma_L^t}{\partial t}$ by approximating the potentials in (8) by reference potentials and solving the resulting linear equation. We improve this strategy with the following monotonicity-based constraints. By observing the ventilation-induced signals in Fig.1 (c), it is reasonable to assume that σ_L^t is monotone with respect to t in the sense that the ventilation-induced conductivity is either increasing everywhere,

$$\frac{\partial}{\partial t}\sigma_L^t(x) \geq 0 \quad \text{for all } x \in \Omega, \tag{10}$$

or decreasing everywhere,

$$\frac{\partial}{\partial t}\sigma_L^t(x) < 0 \quad \text{for all } x \in \Omega. \tag{11}$$

We should mention that the above monotonicity hypothesis may not always be entirely true for all the cases. However, the monotonicity assumption makes sense when considering pressure changes during inspiration and expiration. During inhalation, air flows into the lungs as a result of decrease in the pressure inside the lungs. As a consequence, the overall effective conductivity in the lungs decreases at inhalation [10], [32]. Similarly, the overall effective conductivity in the lungs increases at exhalation. The use of the monotonicity constraint as a temporal regularization allows to deal with the ill-posed nature of EIT and improve the robustness in reconstruction.

From (8), we have

$$\begin{aligned} &\mathbf{a}^T \frac{d}{dt}\mathbb{V}_L(t)\mathbf{a} \\ &= -\int_\Omega \frac{\partial \sigma_L^t}{\partial t} \nabla \left(\sum_{j=1}^E a_j u_t^j \right) \cdot \nabla \left(\sum_{k=1}^E a_k u_t^k \right) dx \end{aligned} \tag{12}$$

for all vectors $\mathbf{a} = (a_1, \ldots, a_E)^T \in \mathbb{R}^E$. For a symmetric matrix A, we write $A \succeq 0$ if A is semi-positive definite, that is, $\mathbf{a}^T A \mathbf{a} \geq 0$ for all vectors $\mathbf{a}$. We write $A \preceq 0$ if A is semi-negative definite. From (12), we have the following monotonicity relations

$$\inf_{x\in\Omega} \frac{\partial \sigma_L^t}{\partial t}(x) \geq 0 \quad \Rightarrow \quad \frac{d}{dt}\mathbb{V}_L \preceq 0, \tag{13}$$

$$\sup_{x\in\Omega} \frac{\partial \sigma_L^t}{\partial t}(x) \leq 0 \quad \Rightarrow \quad \frac{d}{dt}\mathbb{V}_L \succeq 0. \tag{14}$$

Here, the right sides of (13) and (14) should be understood in the sense of matrix definiteness.

The proposed methods evaluate whether the conductivity of the lungs is in the increasing or decreasing period and reconstruct the lung ventilation-induced conductivity change

$\frac{\partial \sigma_L^t}{\partial t}$ using the additional global monotonicity-based constraint (10), resp., (11).

D. EIT data sources consistency

For the monotonicity-based spatiotemporal EIT imaging, it is necessary to determine the conductivity monotone increase and monotone decrease period. According to (13) and (14), the conductivity increasing period can be determined by evaluating the definiteness of $\frac{d}{dt}\mathbb{V}_L$. However, due to the unknown contact impedances of the current driven electrodes, the tridiagonal elements of $\mathbb{V}_L$ are not reliable for determining the period. Fortunately, we made an interesting observation about EIT data sources consistency through several human experiments. This allows us to determine the monotone increase and monotone decrease period of conductivity.

This observation is obtained by a simple modification of the data $V_L^{j,k}(t)$ based on the equations (7), (8) and the monotonicity assumptions (10) and (11)

$$\widetilde{V}_L^{j,k}(t) := \frac{V_L^{j,k}(t)}{sgn\Big(\int_\Omega \nabla u_0^j \cdot \nabla u_0^k dx\Big)} + \Big(1 - sgn\Big(\int_\Omega \nabla u_0^j \cdot \nabla u_0^k dx\Big)\Big) ave(V_L^{j,k}), \tag{15}$$

where sgn is the sign function and $ave(V_L^{j,k})$ indicates the average of $V_L^{j,k}$ over one period of time. Here, u_0^j is the reference potential, which is the solution of (1) with the conductivity distribution σ^t being replaced by the constant 1. Fig. 2 shows $V_L^{j,k}(t)$ and $\widetilde{V}_L^{j,k}(t)$, which are obtained from human experiment. As shown in Fig. 2 (b), most of $\widetilde{V}_L^{j,k}$ are of the same pattern in terms of increasing and decreasing period.

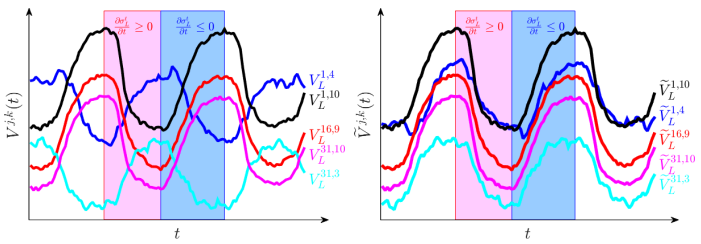

(a) (b)

Figure 2. EIT data obtained from human experiment using 32-channel Swisstom EIT system with 4 skipped injection pattern. (a) band-pass filtered data $V_L^{j,k}$; (b) transformed data $\widetilde{V}_L^{j,k}$ by formula (15).

Several human experiments (seven adults in our lab) and numerical experiments showed that the time change of $\widetilde{V}_L^{j,k}$ is closely related to that of σ_L^t. The modified data $\widetilde{V}_L^{j,k}$ (except a few pair of (j,k)) are consistent with σ_L^t as shown in Fig. 2 (b). It is likely that the inconsistent data in $\widetilde{V}_L^{j,k}$ is related to $\frac{\int_\Omega \nabla u_0^j \cdot \nabla u_0^k dx}{\int_\Omega |\nabla u_0^j \cdot \nabla u_0^k| dx} \le c$ for a constant $c < 0$, meaning that the negative sensitivity overwhelm positive sensitivity by some amount. In Fig. 2, the blue rectangular area indicates the period of decrease in conductivity ($\frac{\partial \sigma_L^t}{\partial t} \le 0$), where $\frac{d}{dt}(\sum_{j,k} \widetilde{V}_L^{j,k}(t)) \ge 0$. On the other hand, the pink rectangular area indicates the period of increase in conductivity ($\frac{\partial \sigma_L^t}{\partial t} \ge 0$), where $\frac{d}{dt}(\sum_{j,k} \widetilde{V}_L^{j,k}(t)) \le 0$.

The consistency between modified data $\widetilde{V}_L^{j,k}$ and conductivity σ_L^t is of great importance to determine the period of increase and decrease in conductivity for imposing temporal regularization constraints. Future studies will be needed to provide a rigorous proof of this observation.

E. Imaging with global monotonicity-based constraints

Discretizing the imaging domain Ω into $\Omega = \cup_{p=1}^N T_p$ where T_p is the p-th pixel, the conductivity distribution σ_L^t in domain Ω can be expressed as $N \times 1$ vector $\boldsymbol{\sigma}_L^t$ (bold symbol). For a vector $\mathbf{b} = (b_1, \ldots, b_N)^T$, we write $\mathbf{b} \ge 0$, resp., $\mathbf{b} \le 0$ if all components of the vector are non-negative, resp., non-positive. From the monotonicity assumption (10), resp., (11), the time differential $\frac{\partial \boldsymbol{\sigma}_L^t}{\partial t}$ satisfies the following uniform positivity (or negativity) property

$$\text{either} \quad \frac{\partial \boldsymbol{\sigma}_L^t}{\partial t} \ge 0 \quad \text{or} \quad \frac{\partial \boldsymbol{\sigma}_L^t}{\partial t} < 0. \tag{16}$$

This paper uses this monotonicity constraint (16) to solve the ill-conditioned linear system (called linearized EIT system) that arises from approximating the potentials in (8) by reference potentials

$$\frac{d}{dt}\mathbf{V}_L = \mathbb{S}\frac{\partial \boldsymbol{\sigma}_L^t}{\partial t}, \tag{17}$$

where $\mathbb{S}$ is the $E^2 \times N$ sensitivity matrix whose $((j-1)*E+k, p)$ element is $S_p^{j,k} = -\int_{T_p} \nabla u_0^j \cdot \nabla u_0^k dx$, and $\mathbf{V}_L(t)$ is the column concatenated data set of $\mathbb{V}_L(t)$ given by

$$\mathbf{V}_L = (V_L^{1,1}, \ldots, V_L^{1,E}, \ldots, V_L^{E,1}, \ldots, V_L^{E,E})^T. \tag{18}$$

We obtain the following global monotonicity-based constrained reconstruction method (GMM)

- In the conductivity increasing period

$$\begin{cases} \min \ \Big\|\mathbb{S}\frac{\partial \boldsymbol{\sigma}_L^t}{\partial t} - \frac{d}{dt}\mathbf{V}_L\Big\|_2^2 + \lambda \|\frac{\partial \boldsymbol{\sigma}_L^t}{\partial t}\|_2^2 \\ \text{subject to} \ \ \frac{\partial \boldsymbol{\sigma}_L^t}{\partial t} \ge 0, \end{cases} \tag{19}$$

- In the conductivity decreasing period

$$\begin{cases} \min \ \Big\|\mathbb{S}\frac{\partial \boldsymbol{\sigma}_L^t}{\partial t} - \frac{d}{dt}\mathbf{V}_L\Big\|_2^2 + \lambda \|\frac{\partial \boldsymbol{\sigma}_L^t}{\partial t}\|_2^2 \\ \text{subject to} \ \ \frac{\partial \boldsymbol{\sigma}_L^t}{\partial t} \le 0, \end{cases} \tag{20}$$

where $\lambda \ge 0$ is the regularization parameter.

In order to implement the minimization problems of (19) and (20), we discretize time t as

$$t_1 < \cdots < t_{n-1} < t_{n+1} < \cdots,$$

and reconstruct the time difference $\boldsymbol{\sigma}_L^{t_n} - \boldsymbol{\sigma}_L^{t_{n-1}}$ by solving the following constrained minimization problems

- In the conductivity increasing period

$$\begin{cases} \min \ \Big\|\mathbb{S}\,(\boldsymbol{\sigma}_L^{t_n} - \boldsymbol{\sigma}_L^{t_{n-1}}) - (\mathbf{V}_L^{t_n} - \mathbf{V}_L^{t_{n-1}})\Big\|_2^2 \\ \qquad +\lambda \|\boldsymbol{\sigma}_L^{t_n} - \boldsymbol{\sigma}_L^{t_{n-1}}\|_2^2 \\ \text{subject to} \ \ \boldsymbol{\sigma}_L^{t_n} - \boldsymbol{\sigma}_L^{t_{n-1}} \ge 0, \end{cases} \tag{21}$$

- In the conductivity decreasing period

$$\begin{cases} \min \ \Big\|\mathbb{S}\,(\boldsymbol{\sigma}_L^{t_n} - \boldsymbol{\sigma}_L^{t_{n-1}}) - (\mathbf{V}_L^{t_n} - \mathbf{V}_L^{t_{n-1}})\Big\|_2^2 \\ \qquad +\lambda \|\boldsymbol{\sigma}_L^{t_n} - \boldsymbol{\sigma}_L^{t_{n-1}}\|_2^2 \\ \text{subject to} \ \ \boldsymbol{\sigma}_L^{t_n} - \boldsymbol{\sigma}_L^{t_{n-1}} \le 0. \end{cases} \tag{22}$$

F. Additional local monotonicity-based constraints

From subsection II-B to subsection II-E, we used a data splitting approach and a monotonicity argument to obtain a global lower (upper) bound for the conductivity change in the conductivity increasing (decreasing) period. In this subsection, we use a refined monotonicity argument to obtain also an upper bound for the conductivity change for the conductivity increasing period(and, analogously, a lower bound for the conductivity decreasing period). The following approach is a new combination of the standard linearized reconstruction method with a sensitivity based variant of the monotonicity method developed in [20]. This is motivated by the recent paper [11] (see also [18]) which uses a sensitivity based variant of the factorization method (see [16], [19], [27]) to regularize the standard linearized reconstruction method.

Given the p-th pixel $T_p \subset \Omega$, define the following $E \times E$ matrix

$$S_p^t = -\begin{bmatrix} \int_{T_p} \nabla u_t^1 \cdot \nabla u_t^1 dx & \cdots & \int_{T_p} \nabla u_t^1 \cdot \nabla u_t^E dx \\ \vdots & \ddots & \vdots \\ \int_{T_p} \nabla u_t^E \cdot \nabla u_t^1 dx & \cdots & \int_{T_p} \nabla u_t^E \cdot \nabla u_t^E dx \end{bmatrix}$$

and note that, for $\mathbf{a} = (a_1, \ldots, a_E)^T \in \mathbb{R}^E$, we have

$$-\mathbf{a}^T S_p^t \mathbf{a} = \int_{T_p} \left| \sum_{j=1}^E a_j \nabla u_t^j \right|^2 dx. \tag{23}$$

We will use the following quantitative version of the monotonicity relations (13) and (14). For $\mathbf{a} = (a_1, \ldots, a_E)^T \in \mathbb{R}^E$,

$$\begin{aligned} &\int_\Omega (\sigma_L^{t_{n-1}} - \sigma_L^{t_n}) \left| \sum_{j=1}^E a_j \nabla u_{t_n}^j \right|^2 dx \\ &\geq \mathbf{a}^T (\mathbb{V}_L(t_n) - \mathbb{V}_L(t_{n-1}))\mathbf{a} \\ &\geq \int_\Omega (\sigma_L^{t_{n-1}} - \sigma_L^{t_n}) \left| \sum_{j=1}^E a_j \nabla u_{t_{n-1}}^j \right|^2 dx, \end{aligned} \tag{24}$$

which is proven in the Appendix B.

Consider the conductivity increasing period, $\sigma_L^{t_{n-1}} \leq \sigma_L^{t_n}$. If $\alpha \geq 0$ fulfills

$$-\alpha \chi_{T_p} \geq \sigma_L^{t_{n-1}} - \sigma_L^{t_n},$$

then, by (23) and (24),

$$\alpha S_p^{t_n} \succeq \mathbb{V}_L(t_n) - \mathbb{V}_L(t_{n-1}),$$

where χ_{T_p} is the characteristic function of subset $T_p \subset \Omega$.

Under the assumption that the conductivity change is constant on the pixel T_p we hence obtain by contraposition that

$$\begin{aligned} &\alpha S_p^{t_n} \not\succeq \mathbb{V}_L(t_n) - \mathbb{V}_L(t_{n-1}) \\ &\qquad \Rightarrow \ (\sigma_L^{t_n} - \sigma_L^{t_{n-1}})|_{T_p} \leq \alpha. \end{aligned} \tag{25}$$

Hence, for p-th pixel we aim to find a smallest possible $\alpha \geq 0$ with $\alpha S_p^{t_n} \not\succeq \mathbb{V}_L(t_n) - \mathbb{V}_L(t_{n-1})$. Collecting the values for all pixels in a vector $\boldsymbol{\alpha}$, we arrive at the following local monotonicity-based constrained reconstruction method (LMM).

- In the conductivity increasing period

$$\begin{cases} \min \ \left\| \mathbb{S}\left(\boldsymbol{\sigma}_L^{t_n} - \boldsymbol{\sigma}_L^{t_{n-1}}\right) - \left(\mathbf{V}_L^{t_n} - \mathbf{V}_L^{t_{n-1}}\right) \right\|_2^2 \\ \qquad +\lambda \|\boldsymbol{\sigma}_L^{t_n} - \boldsymbol{\sigma}_L^{t_{n-1}}\|_2^2 \\ \text{subject to} \ \ \boldsymbol{\alpha} \geq \boldsymbol{\sigma}_L^{t_n} - \boldsymbol{\sigma}_L^{t_{n-1}} \geq 0. \end{cases} \tag{26}$$

Analogously, we obtain for the conductivity decreasing period, $\sigma_L^{t_n} \leq \sigma_L^{t_{n-1}}$, that, for all $\beta \geq 0$,

$$\begin{aligned} &-\beta S_p^{t_{n-1}} \not\preceq \mathbb{V}_L(t_n) - \mathbb{V}_L(t_{n-1}) \\ &\qquad \Rightarrow \ (\sigma_L^{t_{n-1}} - \sigma_L^{t_n})|_{T_p} \leq \beta, \end{aligned} \tag{27}$$

so that we aim to find a smallest possible $\beta \geq 0$ with $-\beta S_p^{t_{n-1}} \not\preceq \mathbb{V}_L(t_n) - \mathbb{V}_L(t_{n-1})$ for p-th pixel and collect the values for all pixels in a vector $\boldsymbol{\beta}$.

- In the conductivity decreasing period

$$\begin{cases} \min \ \left\| \mathbb{S}\left(\boldsymbol{\sigma}_L^{t_n} - \boldsymbol{\sigma}_L^{t_{n-1}}\right) - \left(\mathbf{V}_L^{t_n} - \mathbf{V}_L^{t_{n-1}}\right) \right\|_2^2 \\ \qquad +\lambda \|\boldsymbol{\sigma}_L^{t_n} - \boldsymbol{\sigma}_L^{t_{n-1}}\|_2^2 \\ \text{subject to} \ \ -\boldsymbol{\beta} \leq \boldsymbol{\sigma}_L^{t_n} - \boldsymbol{\sigma}_L^{t_{n-1}} \leq 0. \end{cases} \tag{28}$$

For the implementation of these additional local monotonicity-based constraints, we approximate the potentials u_t^j in the definition of S_p^t by reference potentials u_0^j as this is done in the above-described linearized reconstruction methods. Accordingly, $S_p^{t_n}$ and $S_p^{t_{n-1}}$ are approximated by the matrix S_p, which is obtained by a rearrangement of the p-th column of the sensitivity matrix $\mathbb{S}$ defined in subsection II-E. The smallest possible values for α, resp., β on each pixel are determined by a binary search method.

III. Algorithm summary

The constrained minimization problem with the non-negative constraint (21) and (22) can be viewed as non-negative least square problem [9], [42]. Numerous experiments verified that enforcing a non-negativity constraint could lead to more accurate approximate solution [15], [31]. We adopt algorithm 1 to solve problems (21) and (22).

To solve (26) and (28), we used similar algorithm as solving (21) and (22) with minor modifications of steps ii. 3. (a) and ii. 3. (b) in algorithm 1. Precisely, the step ii. 3. (a) and ii. 3. (b) in algorithm 1 should be adapted as that in algorithm 2.

By adding monotonicity constraints of the conductivity change, the inverse problem will get better posed and the solution of (21), (22) and (26), (28) will provide more accurate and stable images compare with the standard LM. Numerical, phantom and human experiments results will be shown in the following sections.

IV. Numerical simulations

In this section, we show various numerical experiments to test the proposed GMM and LMM and compare the results with that of the standard LM.

Algorithm 1: GMM for EIT reconstruction

i. Initialization: Set $\boldsymbol{\sigma}_L^{t_0} = \boldsymbol{\sigma}_0$ at time $t = t_0$ and solve forward problem (1) to get reference solution u_0 and reference boundary data $\mathbb{V}_L(t_0)$. Compute sensitivity matrix $\mathbb{S}$ with reference solution u_0.

ii. For time $t = t_n$, $n = 1, 2, \ldots$

1. Read measured boundary voltage data $\mathbf{V}(t_n)$
2. Apply band-pass filter to get ventilation-induced signal $\mathbb{V}_L(t_n)$ as well as the time difference data $\mathbb{V}_L(t_n) - \mathbb{V}_L(t_{n-1})$
3. Evaluate the change of $\sum_{j,k} \widetilde{V}_L^{j,k}$ from (15)
   (a) If $\sum_{j,k} \widetilde{V}_L^{j,k}(t_n) \le \sum_{j,k} \widetilde{V}_L^{j,k}(t_{n-1})$, solve the problem (21).
   (b) If $\sum_{j,k} \widetilde{V}_L^{j,k}(t_n) > \sum_{j,k} \widetilde{V}_L^{j,k}(t_{n-1})$, solve the problem (22).
4. Output: For certain given $n \ge 1$, $\boldsymbol{\sigma}_L^{t_n}$ solve problems (21) and (22).

iii. Stop when n reaches the set time step.

Algorithm 2: LMM for EIT reconstruction

ii. 3. (a) If $\sum_{j,k} \widetilde{V}_L^{j,k}(t_n) \le \sum_{j,k} \widetilde{V}_L^{j,k}(t_{n-1})$, compute $\boldsymbol{\alpha}$ by (25) and solve problem (26).

ii. 3. (b) If $\sum_{j,k} \widetilde{V}_L^{j,k}(t_n) > \sum_{j,k} \widetilde{V}_L^{j,k}(t_{n-1})$, compute $\boldsymbol{\beta}$ by (27) and solve problem (28).

A. 2D numerical example

Numerical validation for the proposed monotonicity-based reconstruction methods were performed on a chest model occupying two dimensional domain Ω. See Fig. 3. Three elliptic perturbations were added, one heart modeled in the region $H = \{(x, y) | (x - 3.7)^2 + (y - 1.7)^2 \le 0.7^2\}$ and two lungs modeled in the regions $L_1 = \{(x, y) | \frac{(x-1.8)^2}{0.7^2} + \frac{(y-3)^2}{1.25^2} \le 1\}$ and $L_2 = \{(x, y) | \frac{(x-5.6)^2}{0.7^2} + \frac{(y-3)^2}{1.25^2} \le 1\}$. The conductivity in the regions of H, L_1 and L_2 were set to be time dependent; $\sigma_H^t = 2 + 0.5\cos(3\pi t)$ in H and $\sigma_L^t = 0.5 + 0.3\cos(\pi t)$ in $L_1 \cup L_2$. The background conductivity is 1.

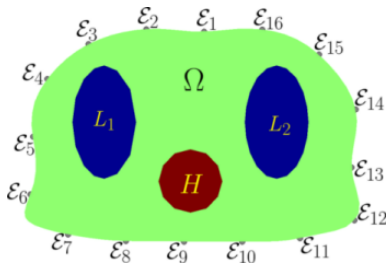

Figure 3. Simulated 16-channel 2D EIT model.

Finite element mesh with 766 triangular elements and 452 nodes was generated. Boundary voltages were simulated using 16-channel EIT system. There are a total of 256 measurements each time frame by injecting currents and measuring boundary voltage adjacently. For simplicity, the contact impedances were ignored in the forward model.

The simulated boundary data $\mathbf{V}$ is separated into two parts by applying band-pass filter, one part $\mathbf{V}_L$ is related to σ_L^t and the other part $\mathbf{V}_H$ is related to σ_H^t. Fig. 4 shows reconstructed images at ten time fames: $t_1 = 0.1, t_2 = 0.3, \ldots, t_{10} = 1.9$. The first row of Fig. shows the true conductivity distributions. The red color in the figure indicates the increasing conductivity or positive values while blue color indicates the decreasing conductivity or negative values. The second row shows EIT images using the standard LM with the unfiltered data $\mathbf{V}$. The third row shows EIT reconstructions using the standard LM with the filtered data $\mathbf{V}_L$. The fourth row shows EIT images using GMM. The fifth row displays images using LMM. Fig. 5 shows images of $\boldsymbol{\alpha}$ and $-\boldsymbol{\beta}$ which are used for LMM in Fig. 4. It shows clearly that $\boldsymbol{\alpha}$ and $-\boldsymbol{\beta}$ provides the upper and lower bound of the conductivity change, respectively. Moreover, numerical experiments with noisy data were conducted. Whiten noise was added to the voltage data to make the signal-to-noise ratio as 50dB. Fig. 6 is the results with the noisy data.

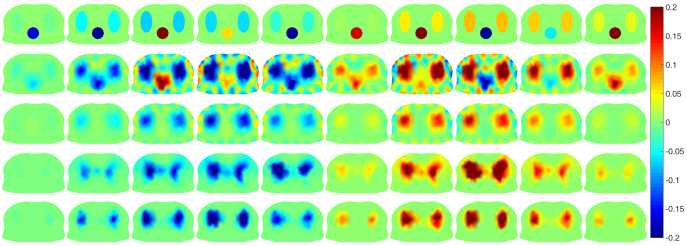

Figure 4. Time-difference conductivity images in the simulated 2D model. (1st row) true distribution of conductivity change; (2nd row) reconstructed images using the standard LM with the unfiltered data $\mathbf{V}$; (3rd row) reconstructed images using the standard LM with the filtered data $\mathbf{V}_L$; (4th row) reconstructed images using GMM; (5th row) reconstructed images using LMM.

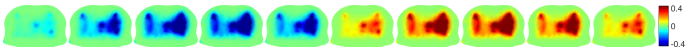

Figure 5. The first five images are $-\boldsymbol{\beta}$ evaluated by the rule (27). The last five images are $\boldsymbol{\alpha}$ evaluated by the rule (25).

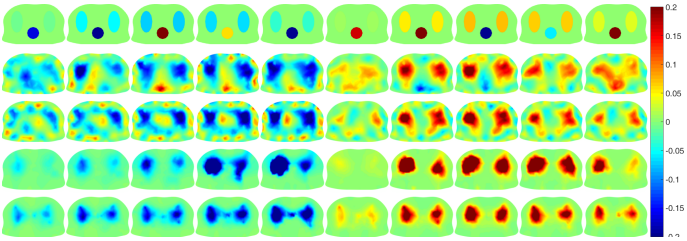

Figure 6. Time-difference conductivity images in the simulated 2D model with whiten noise (SNR=50dB). (1st row) true distribution of conductivity change; (2nd row) reconstructed images using the standard LM with the unfiltered data $\mathbf{V}$; (3rd row) reconstructed images using the standard LM with the filtered data $\mathbf{V}_L$; (4th row) reconstructed images using GMM; (5th row) reconstructed images using LMM.

As shown in Fig. 4 and Fig. 6, results from the standard LM using unfiltered and filtered data have many artifacts. On the other hand, the proposed GMM and LMM provide reconstructions with less artifacts. We chose best regularization λ for the standard LM from many tests by varying λ. For the

proposed GMM and LMM, very small λ was chosen for this simulation and similarly for the subsequent simulations and experiments. Moreover, the performance of GMM and LMM are insensitive to the choice of λ provided λ is sufficiently small. However, the performance of the standard LM is highly depending on the choice of λ. We think the monotonicity constraints play an important role as a temporal regularization in the proposed methods.

B. 3D numerical example

For 3D numerical simulation, thorax model was used as displayed in Fig. 7. To compute the forward solution, 4843 tetrahedra elements and 1195 nodes were used. The thorax model Ω was contained in the cuboid $26cm \times 17cm \times 12cm$, and 32 electrodes were placed as shown in Fig. 7. For each pair of current injection through adjacent electrodes, there are 32 boundary voltage measurements between all pair of adjacent electrodes which lead to a total of 1024 measurements each time frame. Inside the domain Ω, we put two identical cylinders whose size change with time. The size of cylinders at five different times $t_1, \cdots, t_5$ are given in TABLE I. And the vertical center of all the cylinders are at $z = 6cm$. The conductivity value of these two cylinders was set to be 0.5 and background conductivity was 1.

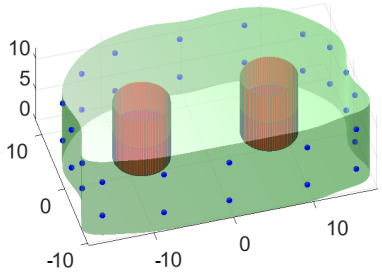

Figure 7. Simulated 32-channel 3D EIT model.

Table I
SIZE OF TWO IDENTICAL CYLINDERS AT FIVE DIFFERENT TIMES.

Time	t_1	t_2	t_3	t_4	t_5
Height	$6cm$	$7cm$	$9cm$	$7cm$	$6cm$
Radius	$1cm$	$2.5cm$	$3.5cm$	$2.5cm$	$1cm$

Fig. 8 and Fig. 9 show EIT reconstructions of xy-slice images at $z = 9cm$ and $z = 3cm$, respectively. The first rows of Fig. 8 and Fig. 9 show the true distribution of conductivity changes. The second rows of Fig. 8 and Fig. 9 show the reconstructed images using the standard LM. The third rows of Fig. 8 and Fig. 9 show reconstructions using GMM. The fourth rows of Fig. 8 and Fig. 9 display the results using LMM.

Fig. 8 and Fig. 9 show that the reconstructions from the standard LM have many artifacts on the background while GMM and LMM have less artifacts. Moreover, the size of reconstructions from LMM are more accurate than that from LM and GMM.

For a quantitative analysis, we evaluated the performance figures of merit including the position error (PE), resolution

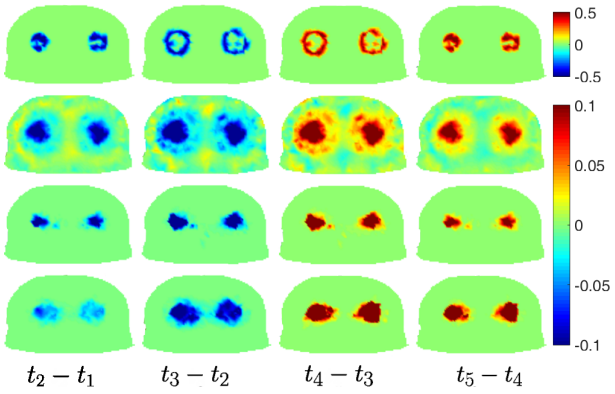

Figure 8. Numerical experiment for time-difference conductivity imaging at the slice $z = 9cm$. (1st row) true distribution of conductivity change; (2nd row) reconstructed images using the standard LM; (3rd row) reconstructed images using GMM; (4th row) reconstructed images using LMM.

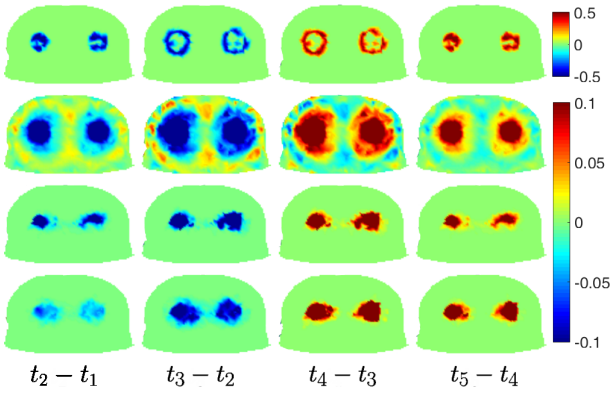

Figure 9. Numerical experiment for time-difference conductivity imaging at the slice $z = 3cm$. (1st row) true distribution of conductivity change; (2nd row) reconstructed images using the standard LM; (3rd row) reconstructed images using GMM; (4th row) reconstructed images using LMM.

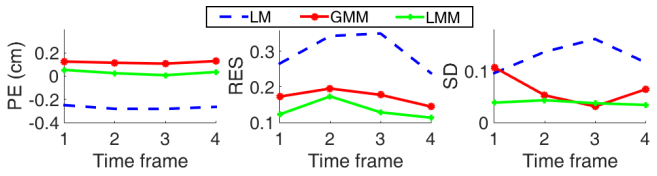

Figure 10. Performance figures of merit [3] for comparison of reconstructed images in Fig. 9: position error (1st column), resolution (2nd column), shape deformation (3rd column).

(RES) and shape deformation (SD) of the reconstructions introduced in GREIT [3]. Fig. 10 shows PE, RES and SD of the results in Fig. 9. The dashed blue lines, red lines and green lines show the results using the standard LM, GMM and LMM, respectively. These quantitative evaluations show that GMM and LMM have better performance than LM since the results from GMM and LMM have less position error, resolution and shape deformation. LMM performs slightly better than GMM as we see from Fig. 8, Fig. 9 and Fig. 10.

V. PHANTOM AND HUMAN EXPERIMENTS

The proposed GMM and LMM were tested with phantom experiments. And for human experiments, results of GMM are

presented. It is difficult to apply the propose LMM to phantom and human experiments, because the tridiagonal elements of the data matrix in (3) as well as in (9) are not reliable due to the unknown contact impedances of the current-driven electrodes. However, we include the reconstructions using LMM of phantom experiments to see how the results are affected by the unknown contact impedances of the current-driven electrodes.

A. Phantom experiments

Experiments were conducted with thorax shape phantom using 32-channel Swisstom pioneer EIT system [45]. To simulate the monotonically conductivity change of the lungs, five well trimmed radishes were used as shown in Fig.11. The detailed information of the size of radishes are shown in TABLE II. The size of thorax phantom is bounded by cuboid $26cm \times 17cm \times 12cm$ with two rings of electrodes. The phantom was filled with saline solution of conductivity $0.32s/m$. 5mA current was injected adjacently at frequency 50kHz and the adjacent boundary voltage data was measured.

The Swisstom EIT system provides a full set of measurements, $V^{j,k}(t), j,k = 1,\ldots,32$ for each time frame. However, the voltage data on current-driven electrodes are known to be prone to errors and affected by unknown contact impedances, so that only 32×29 measurements ($V^{j,k}(t)$ with $|j-k| > 1$) are used for LM and GMM.

Table II
SIZE OF RADISH FOR EXPERIMENTS AT DIFFERENT TIMES.

Time	t_1	t_2	t_3	t_4	t_5
Height	$9.5cm$	$10cm$	$11cm$	$10cm$	$9.5cm$
Radius	$1.5cm$	$2.2cm$	$3.5cm$	$2.2cm$	$1.5cm$

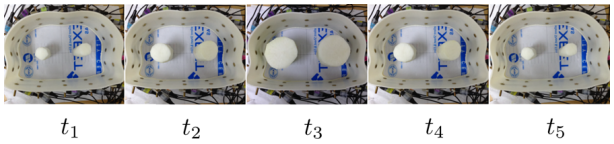

Figure 11. 32-channel EIT phantom.

Fig.12 and Fig.13 display the time difference conductivity images for phantom experiments at slices $z = 9cm$ and $z = 3cm$, respectively. The first rows of Fig.12 and Fig.13 show the reconstructed images using the standard LM. The second rows of Fig.12 and Fig.13 show the reconstructed images using GMM.

Fig.12 and Fig.13 show that even the results from GMM are not perfect, they are relatively good compare with the results from the standard LM considering the shape and position of the objects.

Similar as the quantitative analysis for 3D numerical simulations in Fig. 10, the quantitative evaluation for the phantom experiments are shown in Fig. 14. We see that results from GMM have less position error and shape deformation. The results from LMM and LM have comparative position error and shape deformation.

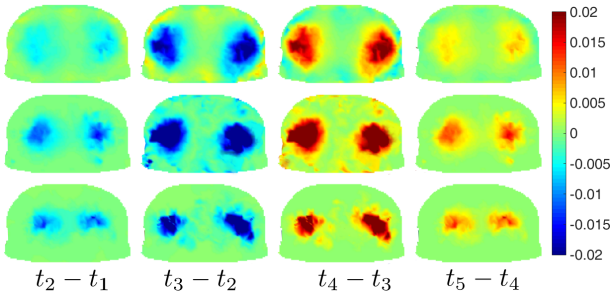

Figure 12. Phantom experiment for time-difference conductivity imaging at the slice $z = 9cm$. (1st row) reconstructed images using the standard LM; (2nd row) reconstructed images using GMM.

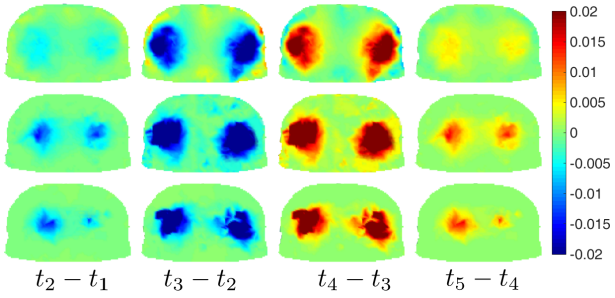

Figure 13. Phantom experiment for time-difference conductivity imaging at the slice $z = 3cm$. (1st row) reconstructed images using the standard LM; (2nd row) reconstructed images using GMM.

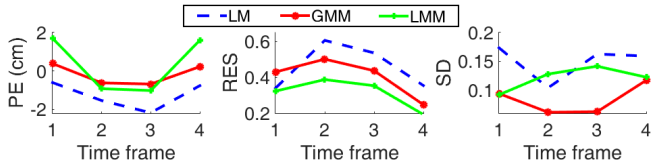

Figure 14. Performance figures of merit [3] for comparison of reconstructed images in Fig. 13: position error (1st column), resolution (2nd column), shape deformation (3rd column).

Please note that the data measured on the current-driven electrodes are removed for the reconstruction of the standard LM and proposed GMM. Full data should be used for the proposed LMM since the LMM requires measurements on the current-driven electrodes. This is a preliminary result to indicate that LMM will also be applicable to real data, but it is not comparable to GMM or LM as the voltage data on driven electrodes are being used for LMM.

We would like to emphasize that it is still an open problem to get reliable full measurements without being affected by the unknown contact impedances of current-driven electrodes. Solving this contact impedance problem is the topic of ongoing research which may rely on two approaches. One approach is the data interpolation using the measured data on the non-current-driven electrodes which is shown in a very recent work [22]. The other approach is to use the compound electrode [24], [44] with which different parts of electrode are used for the current injection and voltage measuring.

B. Human experiments

32-channel Swisstom BB^2 EIT system [46] was used to conduct human experiments. A ring of 32 electrodes were attached to the thorax as shown in Fig. 1 (a). We used the Sense 3D scanner (Cubify 3D System) to scan the 3D geometry of the body. This 3D image with our Matlab GUI software allows us to extract the boundary geometry and electrode positions. See Fig. 15 (a) and (b). Current of 1mA at 150kHz was injected with skipping 4 electrodes, and boundary voltages were measured at 10 frames per second. We applied GMM using a band-pass filtered data surrounding respiratory rate [14]. The source consistency observation in section II-D was used to determine the monotonic increase period and decrease period of conductivity.

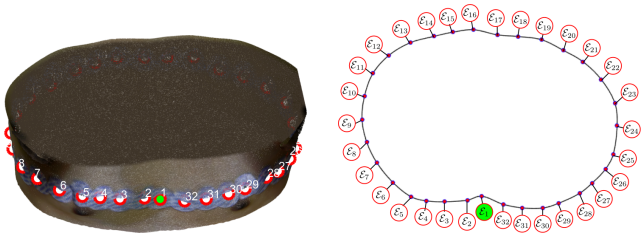

(a) (b)

Figure 15. Automatic object recognition to extract boundary geometry and electrode positions for human experiment. (a) boundary geometry obtained by 3D scanner; (b) electrode positions.

Fig. 16 shows the results using the standard LM and the proposed GMM. The first row of Fig. 16 shows the transformed voltage. The second row shows the reconstruction using the standard LM with unfiltered data $\mathbf{V}$ and the third row shows the results from the standard LM with filtered data $\mathbf{V}_L$. The fourth row of Fig. 16 shows the results from GMM. The dark blue color indicates decease of conductivity while light blue color implies increase of conductivity in the second, third and fourth rows in Fig. 16. We compared the profiles of results from the standard LM and the proposed GMM in the last row of Fig. 16.

Fig. 16 shows that results from GMM have less artifacts than that from the standard LM. The major advantage of the proposed method is its robustness; the reconstructed images are continuously depending on the measured data.

VI. Conclusions

The proposed reconstruction methods allow lung EIT to visualize the monotonically varying conductivity distribution during inhalation and exhalation. It is based on the assumption that lung conductivity monotonically decreases during inhalation (due to the air flowing into the lungs) and monotonically increases during exhalation (due to the air leaving the lungs). The periodicity of lung ventilation is used to extract its associated current-voltage data; all voltage differences between electrodes increase during inhalation and decrease during exhalation in terms of matrix definiteness regardless of the injection currents. This correlation between the time-differential of the current-voltage map and the changes of conductivity can be enforced in the reconstruction algorithm as a constraint.

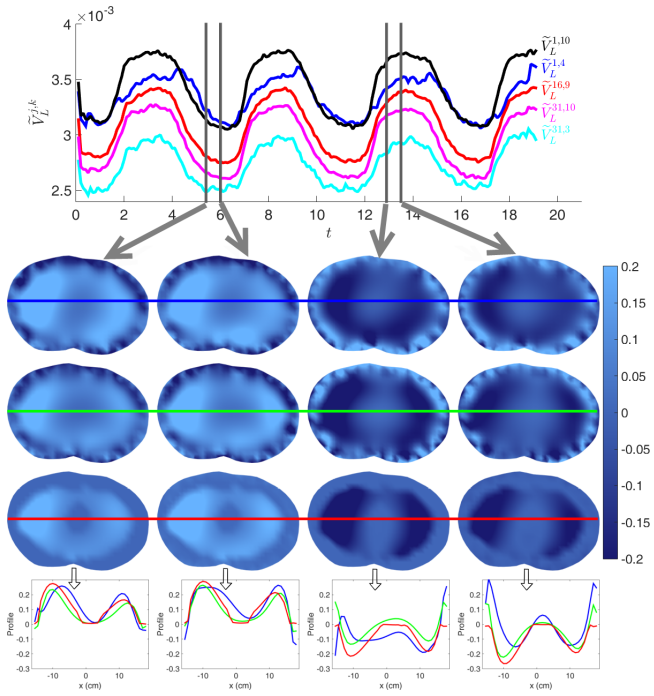

Figure 16. Human experiment. (1st row) transformed voltages using (15); (2nd row) time difference conductivity images using the standard LM with $\mathbf{V}$; (3rd row) LM with $\mathbf{V}_L$; (4th row) GMM; (5th row) their profiles.

We know that the inverse problem of EIT is ill-posed, and therefore any least square method by data-fitting alone may not be able to provide useful images. This means that the boundary current-voltage data alone are insufficient to achieve robust reconstructions for making clinically useful images. Due to the inherent methodological limitation, the EIT reconstruction algorithm requires a strategy that balances data fitting and a suitable regularization by imposing a certain constraint on the expected image. The proposed methods use monotonicity as such a regularization.

Although EIT has limited resolution, its unique advantage lies in its capability for continuous monitoring at the bedside. Given the drawbacks of EIT (e.g., technical difficulties of the ill-posedness related to EIT data being insufficient to probe local conductivity changes), we need to focus on a robust reconstruction method to allow this technique to provide indispensable information in clinical medicine.

Acknowledgment

J. K. Seo and L. Zhou are supported by the National Research Foundation of Korea (NRF) grant funded by the Korean government (MEST) (No. 2011-0028868, 2012R1A2A1A03670512). B. Harrach is supported by the German Research Foundation (DFG) within the Cluster of Excellence in Simulation Technology (EXC 310/1) at the University of Stuttgart.

APPENDIX

A. Proof of the identities (4) and (5).

First note that

$$V^{j,k}(t) = u_t^j|_{\mathcal{E}_k} - u_t^j|_{\mathcal{E}_{k+1}} = \int_{\partial\Omega} u_t^j(\sigma^t \nabla u_t^k \cdot \mathbf{n})ds$$
$$= \int_\Omega \sigma^t \nabla u_t^j \cdot \nabla u_t^k dx,$$

which shows (4) and $V^{j,k}(t) = V^{k,j}(t)$. With the same argument we obtain that

$$V^{j,k}(t) = u_t^j|_{\mathcal{E}_k} - u_t^j|_{\mathcal{E}_{k+1}} = \int_{\partial\Omega} u_t^j(\sigma^{t+\delta t} \nabla u_{t+\delta t}^k \cdot \mathbf{n})ds$$
$$= \int_\Omega \sigma^{t+\delta t} \nabla u_t^j \cdot \nabla u_{t+\delta t}^k dx$$

and

$$V^{j,k}(t+\delta t) = V^{k,j}(t+\delta t) = \int_\Omega \sigma^t \nabla u_t^j \cdot \nabla u_{t+\delta t}^k dx.$$

Hence,

$$\frac{V^{j,k}(t+\delta t) - V^{j,k}(t)}{\delta t} = \int_\Omega \frac{\sigma^t - \sigma^{t+\delta t}}{\delta t} \nabla u_t^j \cdot \nabla u_t^k dx,$$

and it follows that

$$\frac{d}{dt} V^{j,k}(t) = -\int_\Omega \frac{\partial \sigma^t}{\partial t} \nabla u_t^j \cdot \nabla u_t^k dx,$$

which is the asserted identity (5). □

B. Proof of estimate (24).

This type of monotonicity estimate goes back to [25], [26], see also [17], [20], [21] for recent applications.

Let $a_1, \ldots, a_E \in \mathbb{R}$. For brevity, we write $u_t^a := \sum_{j=1}^E a_j u_t^j$. As in the proof of (4) and (5) we have that

$$\mathbf{a}^T \mathbb{V}_L(t_{n-1})\mathbf{a} = \int_\Omega \sigma_L^{t_{n-1}} \nabla u_{t_{n-1}}^a \cdot \nabla u_{t_{n-1}}^a dx,$$
$$\mathbf{a}^T \mathbb{V}_L(t_n)\mathbf{a} = \int_\Omega \sigma_L^{t_n} \nabla u_{t_n}^a \cdot \nabla u_{t_n}^a dx$$
$$= \int_\Omega \sigma_L^{t_{n-1}} \nabla u_{t_{n-1}}^a \cdot \nabla u_{t_n}^a dx.$$

From

$$0 \le \int_\Omega \sigma_L^{t_{n-1}} \left| \nabla u_{t_{n-1}}^a - \nabla u_{t_n}^a \right|^2$$
$$= \int_\Omega \sigma_L^{t_{n-1}} \left| \nabla u_{t_{n-1}}^a \right|^2 - 2\int_\Omega \sigma_L^{t_{n-1}} \nabla u_{t_{n-1}}^a \cdot \nabla u_{t_n}^a$$
$$+ \int_\Omega \sigma_L^{t_{n-1}} \left| \nabla u_{t_n}^a \right|^2$$
$$= \mathbf{a}^T \left(\mathbb{V}_L(t_{n-1}) - \mathbb{V}_L(t_n) \right) \mathbf{a} + \int_\Omega (\sigma_L^{t_{n-1}} - \sigma_L^{t_n}) \left| \nabla u_{t_n}^a \right|^2,$$

it follows that

$$\mathbf{a}^T \left(\mathbb{V}_L(t_n) - \mathbb{V}_L(t_{n-1}) \right) \mathbf{a} \le \int_\Omega (\sigma_L^{t_{n-1}} - \sigma_L^{t_n}) \left| \nabla u_{t_n}^a \right|^2,$$

which is the first inequality in (24). The second inequality in (24) follows from interchanging t_n and t_{n-1}.

REFERENCES

[1] A. Adler and R. Guardo, "Electrical impedance tomography: regularized imaging and contrast detection", *IEEE Trans. Med. Imag.*, vol. 15, no. 2, pp. 170-179, 1996.

[2] A. Adler, R. Guardo and Y. Berthiaume, "Impedance imaging of lung ventilation: do we need to account for chest expansion?", *IEEE Trans. Biomed. Eng.*, vol.43, no.3, pp. 414-420, 1996.

[3] A. Adler , J. Arnold , R. Bayford , A. Borsic , B. Brown , P. Dixon , T. Faes , I. Frerichs , H. Gagnon , Y. Garber , B. Grychtol , G. Hahn , W. Lionheart , A. Malik , R. Patterson , J. Stocks , A. Tizzard , N. Weiler and G. Wolf, "GREIT: A unified approach to 2D linear EIT reconstruction of lung images", *Physiol. Meas.*, vol. 30, pp.S35 -S55, 2009.

[4] H. Ammari (Ed.), "Mathematical modeling in biomedical imaging I: electrical and ultrasound tomographies, anomaly detection, and brain imaging", *Mathematical Biosciences Subseries*, vol. 1983, Springer-Verlag Berlin Heidelberg, pp. 15-25, 2009.

[5] D. C. Barber, B. H. Brown, and I. Freeston, "Imaging Spatial distributions of resistivity using applied potential tomography-APT", *Information Processing in Medical Imaging*, pp. 446-462, Springer Netherlands, 1984.

[6] D. C. Barber and B. H. Brown, "Applied potential tomography", *J. Phys. E: Sci. Instrum.* , vol. 17, no. 9, pp. 723-733, 1984.

[7] I. Bikker, S. Leonhardt, J. Bakker and D. Gommers, "Lung volume calculated from electrical impedance tomography in ICU patients at different PEEP levels", *Intensive Care Med.*, vol. 35, no.8, pp.1362-1367, 2009.

[8] A. Borsic, B. M. Graham, A. Adler and W. R. Lionheart, "In vivo impedance imaging with total variation regularization", *IEEE Trans. Med. Imag.*, vol. 29, no. 1, pp. 44-54, 2010.

[9] R. Bro and S. D. Jong, "A fast non-negativity-constrained least squares algorithm", *Journal of chemometrics*, vol. 11, no. 5, pp. 393-401, 1997.

[10] D. D. Chiras, "Human biology," *Jones & Bartlett Learning, 7th edition*, chapter 8, 2010.

[11] M. K. Choi, B. Harrach and J. K. Seo, "Regularizing a linearized EIT reconstruction method using a sensitivity based factorization method", *Inverse Problems in Science and Engineering*, vol. 22, no. 7, pp. 1029-1044, 2014.

[12] E. Costa, C. Chaves, S. Gomes, M. Beraldo, S. Volpe, M. Tucci, I. Schettino, S. Bohm, C. Carvalho, H. Tanaka, R. Lima and M. Amato, "Real-time detection of pneumothorax using electrical impedance tomography", *Crit. Care Med.*, vol. 36, no. 4, pp. 1230-1238, 2008.

[13] E. Costa, G. Limab and M. Amatoa, "Electrical impedance tomography", *Curr. Opin. Crit. Care*, vol. 15, no. 1, pp. 18-24, 2009.

[14] C. A. Grant, T. Pham, J. Hough, T. Riedel, C. Stocker and A. Schibler, "Measurement of ventilation and cardiac related impedance changes with electrical impedance tomography", *Crit. Care*, vol. 15, no. 1, 2011.

[15] M. Hanke, J. G. Nagy and C. Vogel, "Quasi-Newton approach to nonnegative image restorations," *Linear Algebra Appl.*, vol. 316, no. 1, pp. 223-236, 2000.

[16] M. Hanke and A. Kirsch, "Sampling methods. In handbook of mathematical methods in imaging", *Springer, New York*, pp. 501-550, 2011.

[17] B. Harrach and J. K. Seo, "Exact shape-reconstruction by one-step linearization in electrical impedance tomography", *SIAM J. Math. Anal.*, vol. 42, no. 4, 1505-1518, 2010.

[18] B. Harrach, J. K. Seo and E. J. Woo, "Factorization method and its physical justification in frequency-difference electrical impedance tomography", *IEEE Trans. Med. Imag.*, vol. 29, no. 11, pp. 1918-1926, 2010.

[19] B. Harrach, "Recent progress on the factorization method for electrical impedance tomography", *Comput. Math. Methods Med.* , 2013.

[20] B. Harrach and M. Ullrich, "Monotonicity-based shape reconstruction in electrical impedance tomography", *SIAM J. Math. Anal.*, vol. 45, no. 6, pp. 3382-3403, 2013.

[21] B. Harrach and M. Ullrich, "Resolution guarantees in electrical impedance tomography", *IEEE Trans. Med. Imag.*, vol. 34, no. 7, 2015.

[22] B. Harrach, "Interpolation of missing electrode data in electrical impedance tomography", *Inverse Problems*, vol. 31, no. 11, 2015.

[23] D. Holder, "Electrical impedance tomography: method, history and applications", *Series in Medical Physics and Biomedical Engineering*, CRC Press, December, 2005.

[24] P. Hua, E. J. Woo, J. G. Webster and W.J. Tompkins, "Using compound electrodes in electrical impedance tomography", *IEEE Trans. Biomed. Eng.*, vol. 40, no. 1, pp. 29-34, 1993.

[25] M. Ikehata, "Size estimation of inclusion", *J. Inverse Ill-Posed Probl.*, vol. 6, no. 2, pp. 127-140, 1998.

[26] H. Kang, J. K. Seo and D. Sheen, "The inverse conductivity problem with one measurement: stability and estiation of size", *SIAM J. Math. Anal.*, vol. 28, no. 6, pp. 1389-1405, 1997.
[27] A. Kirsch and N. Grinberg, "The factorization method for inverse problems", *Oxford University Press*, vol. 36, 2008.
[28] P. Kunst, A. Vazquez, S. Böhm, T. Faes, B. Lachmann, P. Postmus and P. Vries, "Monitoring of recruitment and derecruitment by electrical impedance tomography in a model of acute lung injury", *Crit. Care Med.*, vol. 28, no. 12, pp. 3891-3895, 2000.
[29] A. D. Leathard, B. H. Brown, J. Campbell, F. Zhang, A. H. Morice and D. Tayler, "A comparison of ventilatory and cardiac related changes in EIT images of normal human lungs and of lungs with pulmonary emboli", *Physiol. Meas.*, vol. 15, pp. A137-A146, 1994.
[30] T. Meier, H. Luepschen, J. Karsten, T. Leibecke, M. Grossherr, H. Gehring and S. Leonhardt, "Assessment of regional lung recruitment and derecruitment during a PEEP trial based on electrical impedance tomography", *Intensive Care Med.*, vol. 34, no. 3, pp. 543-550, 2008.
[31] J. G. Nagy and Z. Strakos, "Enforcing nonnegativity in image reconstruction algorithms", *In International Symposium on Optical Science and Technology*, International Society for Optics and Photonics, pp. 182-190, 2000.
[32] P. Nopp, N. D. Harris, T. X. Zhao and B. H. Brown, "Model for the dielectric properties of human lung tissue against frequency and air content", *Med. & Biol. Eng. & Comput.*, vol. 35, no.6, pp. 695-702, 1997.
[33] T. I. Oh, H. Koo, K. H. Lee, S. M. Kim, J. Lee, S. W. Kim, J. K. Seo and E. J. Woo, "Validation of a multi-frequency electrical impedance tomography (mfEIT) system KHU Mark1: impedance spectroscopy and time-difference imaging", *Physiol. Meas.*, vol. 29, pp. 295-307, 2008.
[34] C. Putensen, H. Wrigge and J. Zinserling, "Electrical impedance tomography guided ventilation therapy", *Curr. Opin. Crit. Care*, vol. 13, no. 3, pp. 344-350, 2007.
[35] J. K. Seo and E. J. Woo, "Nonlinear inverse problems in imaging", *Wiley, 1st edition*, December, 2012.
[36] E. Somersalo, M. Cheney and D. Isaacson, "Existence and uniqueness for electrode models for electric current computed tomography", *SIAM J. Appl. Math*, vol. 52, no. 4, pp. 1023-1040, 1992.
[37] A. Tamburrino, "Monotonicity based imaging methods for elliptic and parabolic inverse problems", *J. Inverse Ill-Posed Probl.*, vol. 14, no. 6, pp.633-642, 2006.
[38] A. Tamburrino and G. Rubinacci, "A new non-iterative inversion method for electrical resistance tomography", *Inverse Problems*, vol. 18, no. 6, pp. 1809-1829, 2002.
[39] E. Teschner and M. Imhoff, "Electrical impedance tomography: the realization of reginal ventilation monitoring", *Dráger. Technology for Life*, 2011.
[40] M. Vauhkonen, D. Vadasz, P. A. Karjalainen, E. Somersalo and J. P. Kaipio, "Tikhonov regularization and prior information in electrical impedance tomography", *Tran. Med. Imag.*, vol. 17, no. 2, pp. 285-293, 1998.
[41] P. J. Vauhkonen, M. Vauhkonen, T. Savolainen J. P. Kaipio, "Three-dimensional electrical impedance tomography based on the complete electrode model", *IEEE Trans. Biomed. Eng.*, vol. 46, no. 9, pp. 1150-1160, 1999.
[42] C. R. Vogel, "Computational methods for inverse problems", *SIAM*, Philadelphia, USA, 2002.
[43] G. Wolf, C. Gomez-Laberge, J. Rettig, S. Vargas, C. Smallwood, P. Prabhu, S. Vitali, D. Zurakowski and J. Arnold, "Mechanical ventilation guided by electrical impedance tomography in experimental acute lung injury", *Crit. Care Med.*, vol. 41, no. 5, pp. 1296-1304, 2013.
[44] E. J. Woo, P. Hua, J. G. Webster, W. J. Tompkins and R. P. Areny, "Skin impedance measurements using simple and compound electrodes", *Med. & Biol. Eng. & Comput.*, vol. 30, no. 1, pp. 97-102, 1992.
[45] Brochure for Swisstom EIT Pioneer Set, http://www.swisstom.com/wp-content/uploads/Swisstom_brochure-PioneerSet_GB_1ST500-102_Rev002_web.pdf, Swisstom AG, 2015.
[46] Watch the lungs breathe! EIT real-time monitoring with Swisstom BB^2, http://www.swisstom.com/wp-content/uploads/SwisstomBB2_Brochure_GB_2ST100-112_Rev003.pdf, Swisstom AG, 2015.